Decoding the Role of CeO_2 in Enhancing Oxygen Reduction Activity of CuO/C Nanostructures

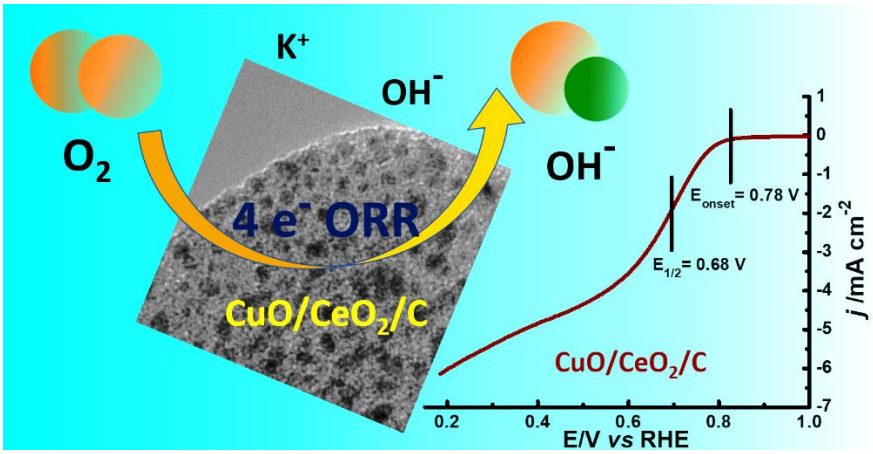

A facile two-step solvothermal synthesis of a heterostructure of $CuO/CeO_2/C$ for ORR electrocatalysis is discussed in this chapter. The EC possessed surface oxygen vacancies, oxide-carbon interfaces, high specific surface area and high ECSA as revealed by XPS, Raman, TEM, BET and electrochemical results. A study with various electrochemical performances exhibited by $CuO/CeO_2/C$ establishes that it acts as a high-performance and stable EC toward ORR in an alkaline medium. All the experimental methodologies for the synthesis, physicochemical and electrochemical characterization used in this chapter were discussed in Chapter 2.

4.1. Introduction

Numerous TMO-based materials including oxides of Mn, Fe, Cu, Co, Ni etc. have been considerably inspected as cost-effective ORR/OER ECs for PEMFCs and MABs [1–3]. Among them, CuO_x with its unique redox properties has attracted significant attention because of its high ORR activity, low cost and easy availability in nature [4,5]. However, other non-precious metal-oxides have also been found to be potential options as EC material, because of their highly abundant nature than noble metals like Pt, Ru, Ir etc. Benefiting from these advantages, this class of materials have been extensively investigated as EC for future hydrogen energy technologies such as

FCs, MABs or electrolyzers. To increase the intrinsic electrocatalytic activity of the non-noble metal oxide-based materials, various structural engineering approaches have been developed. Recently, CeO_2-promoted TMOs anchored on carbon have been used as bifunctional ECs for ORR and OER in alkaline solutions [6–9]. CeO_2 has exceptional features with high oxygen storage transport capability because of its unique Ce^{4+}/Ce^{3+} redox couple. The oxygen defects arising from CeO_2 allow the exposer of the active sites of the TMO compounds adjusting the quick transfer of the molecular O_2, endorsing the synergy that can enhance the ORR/OER activity. Similarly, Carbon materials such as CNT, Vulcan XC 72R, rGO, KB etc. have been extensively explored as electrode components for FCs and MABs [10–13]. Carbon-based materials display exceptional conductive properties and act as excellent support which can enhance the performance of electrocatalytically active metal sites. The last chapter (Section-3A and Section-3B) illustrate the morphological and structure-activity characteristics of Co_3O_4-based (Oct- Co_3O_4/C and Sp-Co_3O_4/C) ECs for ORR and OER in alkaline solution. In this chapter, taking into account the demands of high electrocatalytic activity with greater energy storage and conversion technologies, the intrinsic ORR electrocatalytic activity of carbon-supported CuO has been explored with the addition of CeO_2 promoter/support.

4.2. Results and Discussion

4.2.1. Structural and morphological characterization

The structure, crystallinity and phase purity in the synthesized ECs were studied by using powder XRD analysis. Figure 4.1. a show the XRD patterns of Vulcan carbon, CeO_2/C, CuO/C and $CuO/CeO_2/C$. The broad and low-intensity XRD peak at about 24^o (2θ) revealed by the Vulcan carbon is the characteristic of graphitic sp^2 carbon structure [14]. The carbon peak disappears in the case of CuO/C, $CuO/CeO_2/C$ and CeO_2/C because of the high dispersion of MO phases into the carbon latices that lowers the crystallinity of the carbon material. While for CeO_2/C, it shows a clear diffraction pattern of pure CeO_2 which is consistent with the standard JCPDS No. 81-0792. Similarly, CuO/C shows the diffraction patterns of pure CuO in accordance with JCPDS No. 89-5895. The $CuO/CeO_2/C$ sample exhibited mixed diffraction peaks of CuO and CeO_2 suggesting the coexistence of the hybrid oxides. This study demonstrates that there exists a partial and random interfacial overlapping

phase in between all the CeO_2 and CuO phases instead of dispersion of CuO phases into the CeO_2 lattice. The change in the peak intensity and peak broadening observed for the mixed oxide further establishes the incorporation of overlapping oxide-oxide interfaces of the CeO_2 and CuO phases.

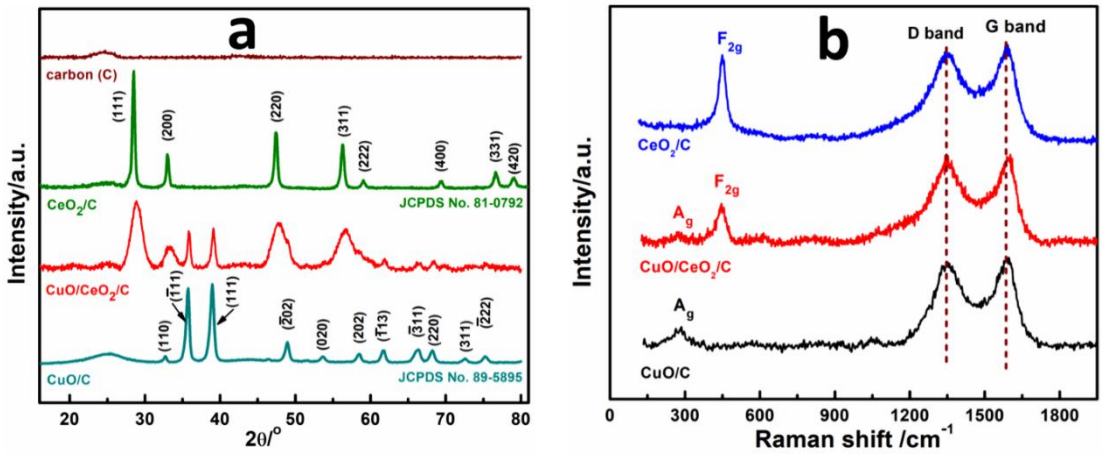

Figure 4.1. a) XRD patterns of Vulcan carbon, CeO_2/C, CuO/CeO_2/C and CuO/C, b) Raman spectra of CeO_2/C, CuO/CeO_2/C and CuO/C.

To study the structural changes, defect nature and the effect of CeO_2 concentration in the CuO/CeO_2/C mixed oxide, Raman spectroscopic analysis has been performed. Figure 4.1. b shows the Raman spectra of CeO_2/C, CuO/C and CuO/CeO_2/C. The Raman spectra of single CeO_2/C show a sharp peak at about 454 cm^{-1} which is ascribed to the symmetric F_{2g} mode for *fcc* CeO_2 due to the symmetric O–Ce–O stretching over the surrounding oxygen atoms of the fluorite structured CeO_2 [15,16]. Xin and co-workers investigated Raman spectra of CuO NPs with various crystalline sizes to establish the relation between Raman intensity and particle size [17]. It is reported that the smaller crystallite size of CuO shows sharper and intensified Raman peaks with redshift. The significant peak broadening and reduction of the peak intensity of A_g (286 cm^{-1}) and F_{2g} (450 cm^{-1}) Raman peaks observed for CuO/CeO_2/C relative to that of the parent CuO/C and CeO_2/C are due to the heterogeneous interfacial structure in the mixed compound. It further establishes the facilitation of more oxygen in the mixed structure [18].

The elemental analysis along with the Wt.% and At.% of the synthesized ECs was accomplished by EDX analysis which demonstrates the exclusive elements

present in the ECs (Figure 4.2). The At.% of Cu, Ce, O and C in CuO/CeO_2/C were 0.52, 0.60, 16.75 and 82.13 % respectively.

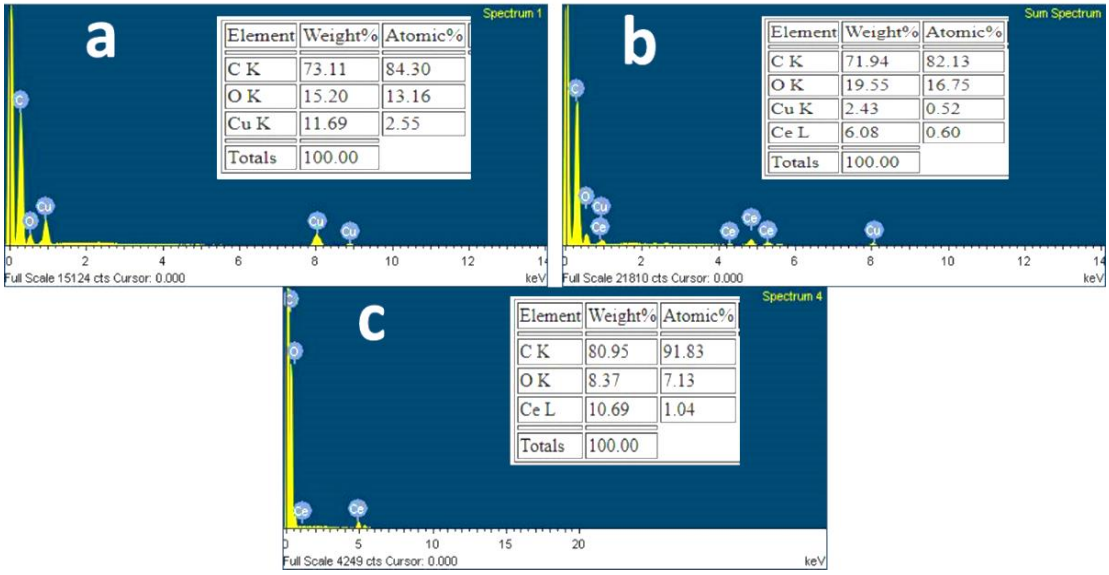

Figure 4.2. EDX spectra of the ECs. a) CuO/C, b) CuO/CeO_2/C and c) CeO_2/C. The Tables in the inset of the respective images represent the At.% And Wt.% of the elements.

The particle size and the morphological texture of CuO and CeO_2 NPs in CuO/CeO_2/C were studied by the TEM imaging technique. The low-resolution TEM image as shown in Figure 4.3. a and b reveals that the particles are in the nano-dimensional range. The average particle size was calculated from the TEM images and observed to be around 2.5 to 3 nm. Figure 4.3. c shows the HRTEM image of the CuO/CeO_2/C which reveals the typical lattice spacing for both CuO and CeO_2. CuO shows the characteristics lattice spacing of 0.23 and 0.27 nm corresponding to (111) and (110) crystal planes, respectively, while CeO_2 reveals its characteristics lattice spacing of about 0.31 nm corresponding to the (111) crystal plane which is consistent with the XRD and SAED results [19,20]. The SAED pattern of CuO/CeO_2/C further reveals a relatively better crystallinity and the presence of different phases in several orientations (Figure 4.3. d).

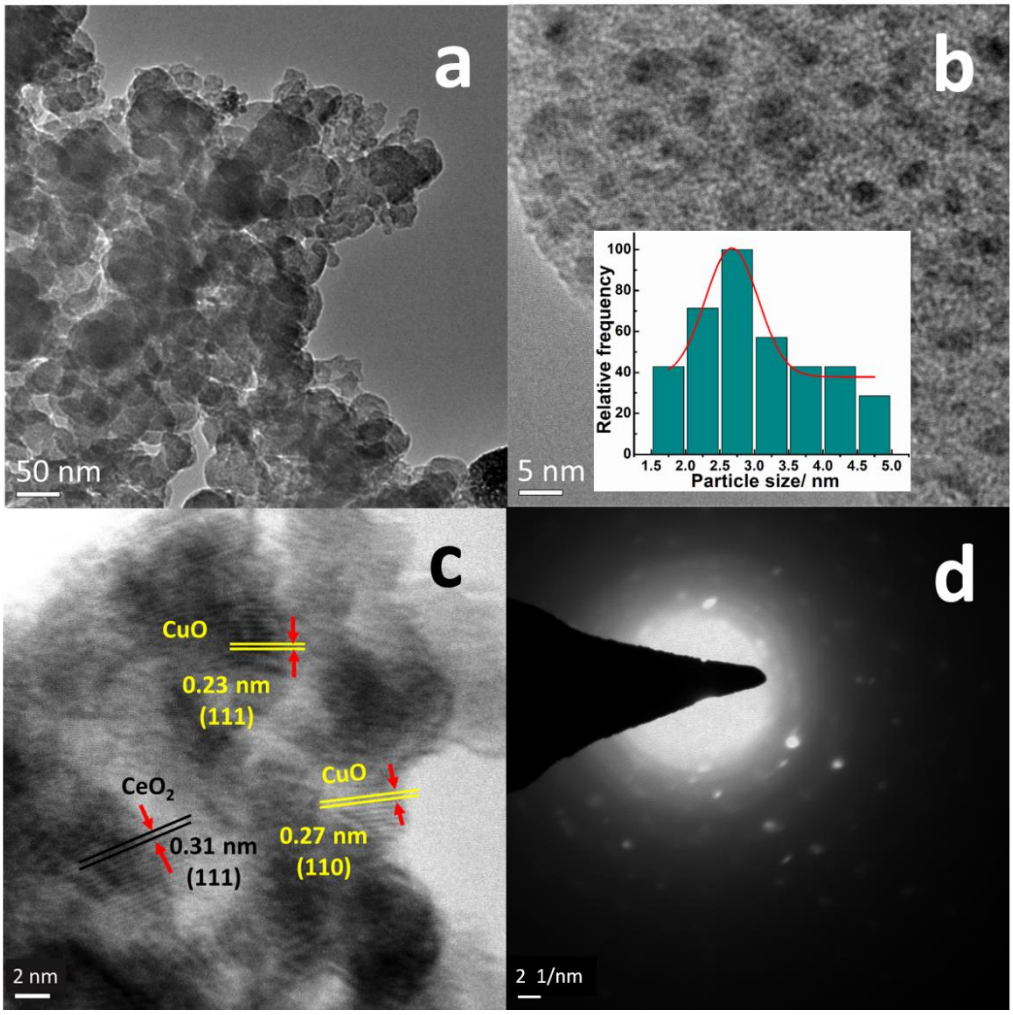

Figure 4.3. a, b) TEM images of $CuO/CeO_2/C$ (inset of b shows the particle size distribution), c) HRTEM image and d) SAED pattern of $CuO/CeO_2/C$.

The XPS spectra further reveal the chemical compositions of metal valence states along with the surface O and C states in the carbon-supported CuO/CeO_2. The survey spectrum of $CuO/CeO_2/C$ is shown in Figure 4.4. a which displays the relative peak intensities and the relative peak positions of the Cu 2p, Ce 3d, O 1s, and C 1s XPS spectra of the EC. The core level Cu 2p XPS spectra show a lower and a higher energy band separated by spin-orbit splitting energy of 19.85 eV along with the typical satellite peaks at 938.6 and 943.3 eV as displayed in Figure 4.4. b, which are characteristics of the CuO structure [20]. Figure 4.4. c shows the deconvolution of O 1s spectra that reveals the chemisorbed oxygen species (O_{ads}) and the lattice oxygen (O_{lat}). The peak at 532.4 eV corresponds to O_{ads}, whereas the peak at 529.6 eV can be

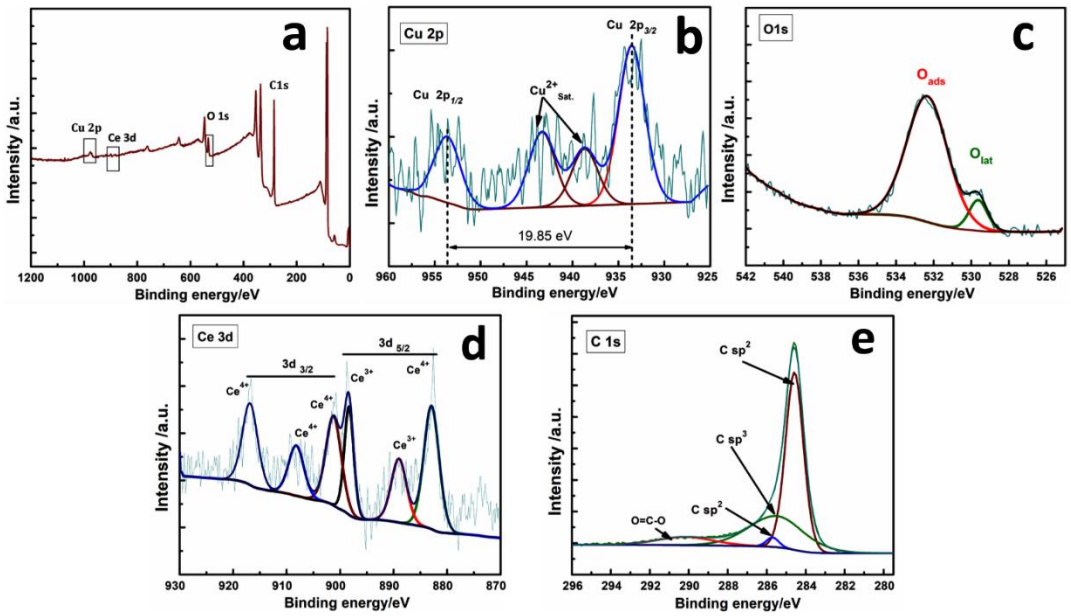

Figure 4.4. a) XPS survey spectrum, b) core-level Cu 2p, c) O 1s, d) core level Ce 3d and d) C 1s XPS spectrum of $CuO/CeO_2/C$.

assigned to O_{lat} [21]. The core level Ce 3d XPS spectra produce two sets of peaks, which are assigned to $3d_{3/2}$ and $3d_{5/2}$ as shown in Figure 4.4. d. The Ce in CeO_2 exists as Ce^{3+} and Ce^{4+} oxidation states. The peaks at 889 and 898.4 eV in the XPS spectrum are assigned to Ce^{3+} while the peaks at 882.9, 901.2, 908.2, and 916.9 eV are assigned to the Ce^{4+} state of cerium [22,23]. The existence of the Ce^{3+} population signifies the accumulation of oxygen vacancies in the mixed oxide EC. The % composition of Ce^{3+} and Ce^{4+} was calculated to be 27.35 and 72.65 %, respectively. This study demonstrates that the $CuO/CeO_2/C$ mixed oxide is integrated with sufficiently rich oxygen vacancies that might carry a significant role in the ORR process. Figure 4.4 e shows the deconvolution of the C 1s spectrum which reveals the population of sp^3 and sp^2 C-states. The sp^2 C indicates the graphitic carbon concentration in the EC which is consistent with the XRD and Raman results.

The specific surface area and pore-size distribution of the series of investigated ECs were studied by BET and BJH methods. N_2 adsorption-desorption isotherm shows the typical type-IV isotherm and H3-type hysteresis loop as displayed in Figure 4.5 a-c. It is observed that $CuO/CeO_2/C$ possesses a significantly higher specific surface area (153.7 $m^2\ g^{-1}$) than that of CuO/C (118.4 $m^2\ g^{-1}$) and CeO_2/C (86.4 $m^2\ g^{-1}$).

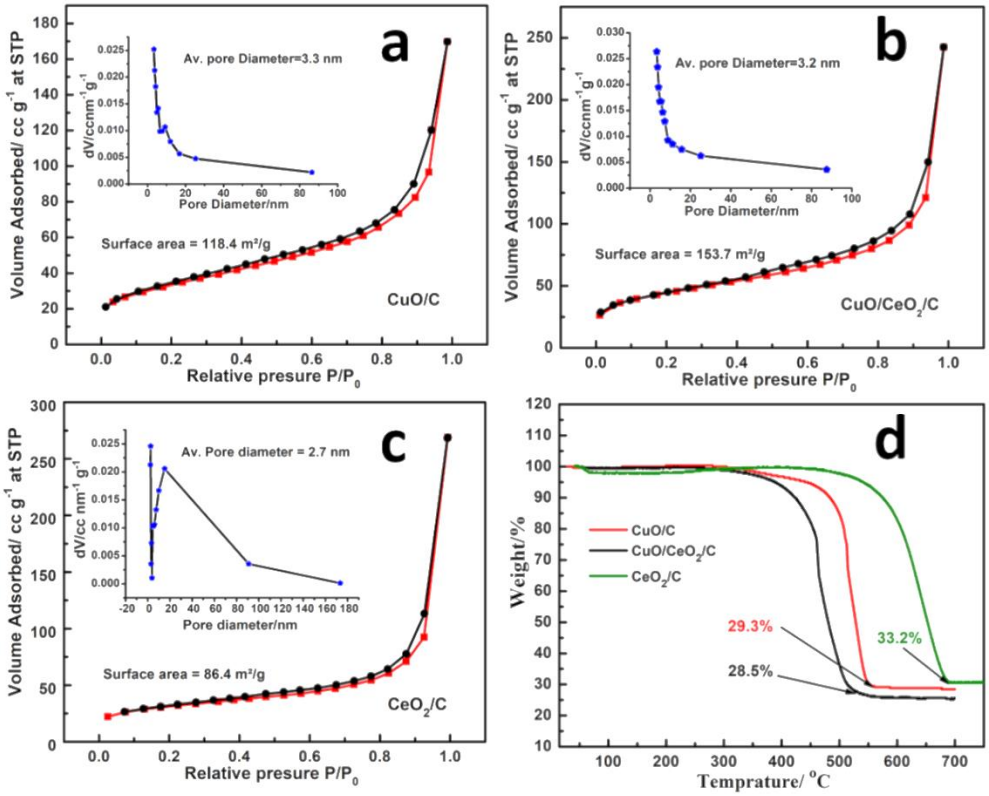

Figure 4.5. N_2 adsorption-desorption isotherms of (a) CuO/C, (b) $CuO/CeO_2/C$ and (c) CeO_2/C hybrid (the inset displays the corresponding pore size distribution curves), and (d) TGA profile of CuO/C, $CuO/CeO_2/C$ and CeO_2/C in air atmosphere.

The insets of Figure 4.5 a-c display the respective pore size distribution curves, obtained by the BJH method. The pore sizes for CuO/C, $CuO/CeO_2/C$ and CeO_2/C were calculated to be 3.3, 3.2 and 2.7, respectively which suggests the characteristics of the mesoporous nature of the ECs. The TGA analysis shows the decay of carbon mass from the ECs as a function of temperature (Figure 4.5 d). It is observed that the TGA curves get stable after the loss of ~70 Wt.% which is due to the decomposition of carbon mass into CO_2 at higher temperatures. The residual ~30 Wt.% is the MO fraction of the catalysts which establishes the intended 30 Wt.% MO content in the ECs.

4.2.2. Electrocatalytic Activity towards ORR

The ORR activities of the as-prepared nanostructures were first evaluated by CV in both N_2- and O_2-saturated 0.1 M KOH solution using a GC electrode. Figure 4.6 a-c shows the CV scans for CuO/C, $CuO/CeO_2/C$ and CeO_2/C, respectively. The

reduction peaks observed in the CVs under O_2-saturated environment are exclusively due to the redox reaction of O_2 only as under N_2- saturated atmosphere no significant redox peak was observed. All the ECs show significant electrocatalytic activity towards ORR. Notably, the incorporation of CeO_2 into CuO/C made the mixed EC different in action towards electrocatalytic activity, CV loop, onset potential as well as peak potential. The ORR onset potential for CuO/C and CeO_2/C were observed to be 0.72 and 0.75 V (vs. RHE), respectively while for CuO/CeO_2/C, it was found to

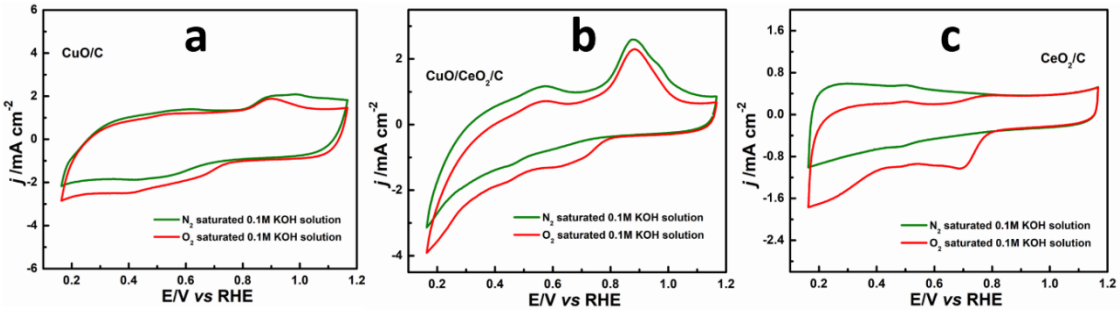

Figure 4.6. a) CVs of CuO/C, b) CuO/CeO_2/C and c) CeO_2/C in N_2 and O_2-saturated 0.1 M KOH solution at a scan rate of 50 mV s^{-1}.

be 0.78 V. The observed positive shift suggests the overpotential drop for ORR with CuO/CeO_2/C. The fundamental evaluation of ORR activity by CV study shows the significant promotion effect of CeO_2 in CuO/CeO_2/C. To further explore the ORR pathways and the kinetics catalyzed by the prepared ECs, RDE measurements were performed. Figure 4.7 a-c presents the LSV polarization curves of CuO/C, CuO/CeO_2/C and CeO_2/C measured at different rpm in O_2-saturated 0.1 M KOH solution. The trends in the electrocatalytic activity of the catalysts are comparable to those found in the CV study. Based on the measured LSV polarization curves at various rpm, the number of electrons (n) involved in a single ORR cycle is evaluated employing Koutecky-Levich (K-L) equation [24].

The linear fitting lines of the K-L plots for CuO/C, CuO/CeO_2/C and CeO_2/C are presented in Figure 4.7.d-f, respectively. It is observed that electrocatalysis over both CuO/C and CuO/CeO_2/C proceeds via a direct $4e^-$ reduction pathway without the formation of any O_2^{2-} intermediate, whereas the CeO_2/C exhibit an indirect reduction pathway (n =2.4) facilitating sort of intermediates. The linearity and parallel fitting

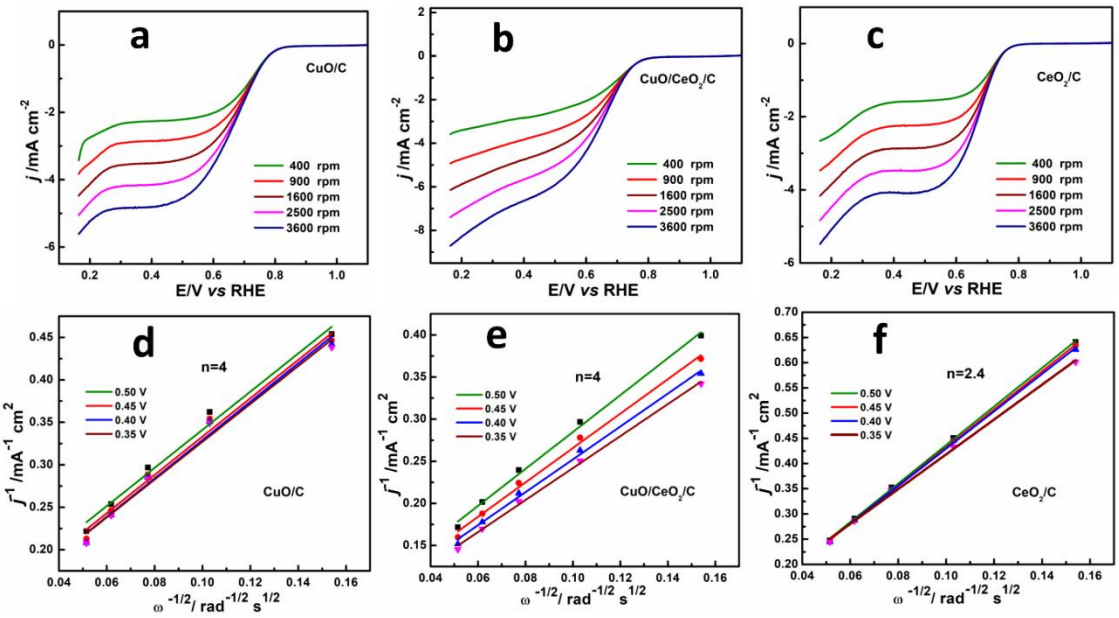

Figure 4.7. ORR polarization curves of a) CuO/C, b) CuO/CeO_2/C and c) CeO_2/C in O_2-saturated 0.1 M KOH solution at a sweep rate 5 mV s^{-1}, K–L plots of a) CuO/C, b) CuO/CeO_2/C and c) CeO_2/C at 0.35, 0.40, 0.45 and 0.50 V (the 'n' values are calculated at 0.40 V).

lines of the K-L plots at diffusion-controlled and mixed kinetic diffusion-controlled potential regions of the LSV curves recommend first-order kinetics of the studied ORR ECs [25,26]. These observations further suggest a similar number of electrons transferred at all recorded RDE rotations during the ORR for the respective ECs.

Figure 4.8 a shows the LSV polarization curves portraying the relative current densities and E_{onset} for the investigated ECs at 1600 rpm. Vulcan carbon exhibits a significantly poor E_{onset} and lower current density in the less positive potential region, while the integration of CuO results in a higher current density and more positive ORR E_{onset} (0.72 V). Similarly, CeO_2/C has also exhibited higher ORR activity compared to that of bare carbon. However, when it is investigated for the CuO/CeO_2/C, it shows more positive E_{onset} (0.78 V) and $E_{1/2}$ (0.68 V) which is satisfactorily higher than those of the CuO/C and CeO_2/C. Moreover, the limiting current density of CuO/CeO_2/C at 1600 rpm is −6.14 mA cm^{-2} which is reasonably higher than the CuO/C (−4.47 mA cm^{-2}), CeO_2/C (−4.14 mA cm^{-2}). This signifies a synergistic action on the addition of CeO_2.

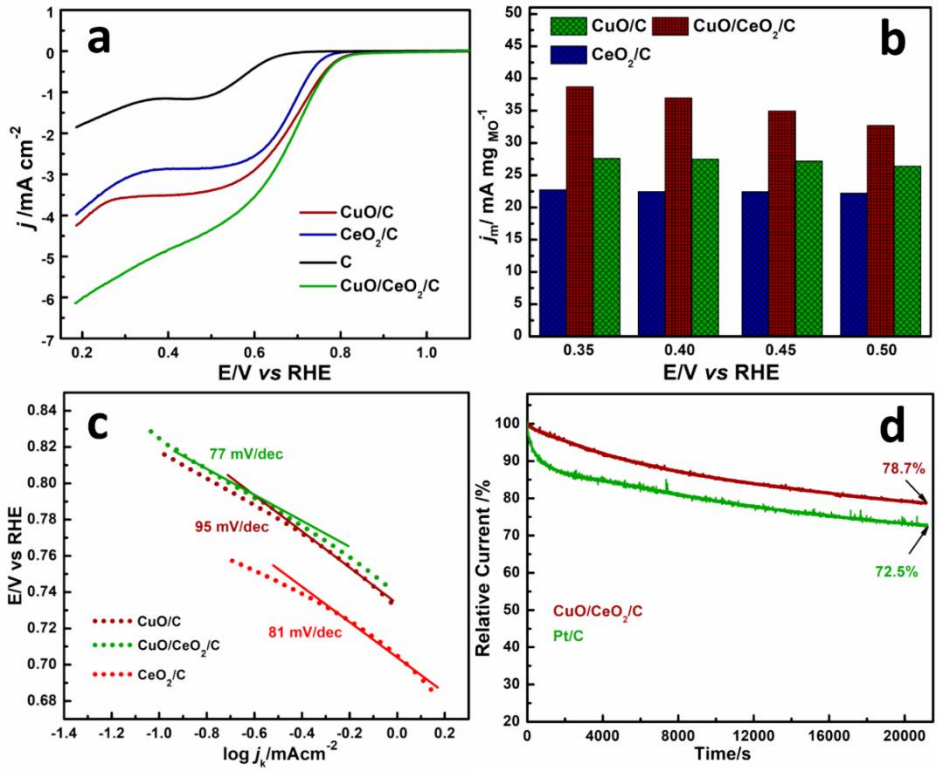

Figure 4.8. Electrocatalytic ORR performance of the ECs. a) LSV polarization curves of carbon, CuO/C, CuO/CeO_2/C and CeO_2/C at 1600 rpm, b) mass-specific activity of CuO/C, CuO/CeO_2/C and CeO_2/C, c) ORR Tafel slope and d) chronoamperometric test upto 6 h for CuO/CeO_2/C and Pt/C.

Figure 4.8 b shows the mass activity of the ECs at 1600 rpm over the potential range of 0.35-0.50 V. It shows the trends in ORR activity in order of CuO/CeO_2/C > CuO/C > CeO_2/C which suggests the enhanced intrinsic activity of the CuO/CeO_2/C. Figure 4.8 c presents the Tafel slopes for the investigated ECs. CuO/CeO_2/C exhibits a faster ORR kinetics with a lower Tafel slope (77 mV dec^{-1}) in comparison to that of CuO/C (95 mV dec^{-1}) and CeO_2/C (81 mV dec^{-1}). The chronoamperometric test shows the ORR operational stability of CuO/CeO_2/C as displayed in Figure 4.8 d. It is observed that CuO/CeO_2/C possesses higher retention of its initial current of 78.7% than that of Pt/C which shows 72.5% of its initial current after the 6 h of chronoamperometric operation.

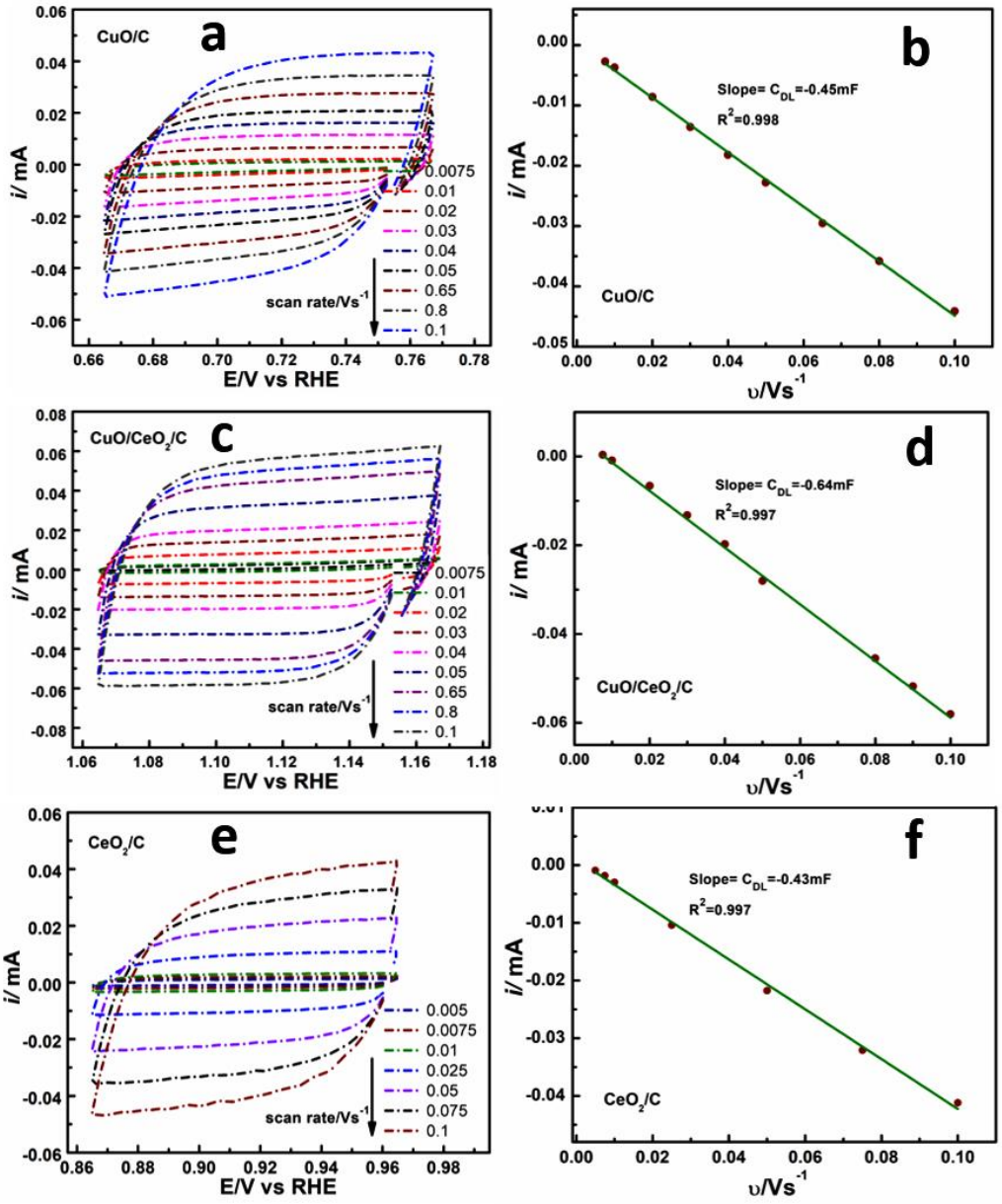

Figure 4.9. C_{dl} measurements for determining ECSA in 0.1 M KOH. Left panel (a,c,e) represents CVs of CuO/C, CuO/CeO_2/C and CeO_2/C at various scan rates. The right panel (b,d,f) is the slope obtained from respective CV data.

The ECSA of the samples is evaluated by employing CV derived double layer capacitance (C_{dl}) method at a non-faradaic potential region. Figure 4.9 show the CVs of CuO/C, CuO/CeO_2/C and CeO_2/C at various scan rates and the corresponding slope current vs. scan rate from which the C_{dl} and ECSA value can be evaluated. The ECSA of CuO/C, CuO/CeO_2/C and CeO_2/C are calculated to be 37.5, 53.32 and 35.8 m^2g^{-1}, respectively.

The inclusive investigation suggests that the prepared $CuO/CeO_2/C$ mixed oxide demonstrated excellent activity toward ORR in alkaline conditions. Recognising the roots of the enhanced ORR electrocatalysis for the $CuO/CeO_2/C$ versus the individual parent counterparts (i.e., CuO/C and CeO_2/C), offers insightful assistance in scheming material design for ORR electrocatalysis. The HRTEM image (Figure 4.3. c) shows that $CuO/CeO_2/C$ acquired a heterogeneous interfacial structure of CuO, CeO_2 and C with the characteristics lattice spacing of CuO-(111), CuO-(110) and CeO_2-(111) crystal planes. The interfacial domains facilitate more catalytic active sites and offer more spaces for O_2 adsorption and desorption. The high BET surface area $CuO/CeO_2/C$ has also a critical impact on the enhanced ORR activity. In addition, $CuO/CeO_2/C$ possesses higher ECSA as compared to that of the single CuO/C and CeO_2/C which could be demonstrated as a key factor for the improved electrocatalytic activity of $CuO/CeO_2/C$. Furthermore, XPS measurements reveal the valence states of Ce^{4+} and Ce^{3+} in $CuO/CeO_2/C$ which shows the coexistence of the Ce^{4+}/Ce^{3+} redox couple. With the assistance of the Ce^{4+}/Ce^{3+} redox mechanism, CeO_2 can enhance the intrinsic activity of CuO as it can reserve O_2 in an O_2-rich atmosphere and release it in O_2 deficiency conditions.

4.3. Conclusions

In summary, CuO/C, $CuO/CeO_2/C$ and CeO_2/C nanostructures were successfully synthesised by a solvothermal route to investigate the electrocatalytic activity for ORR an alkaline medium. $CuO/CeO_2/C$ possesses a more positive E_{onset} and $E_{1/2}$, which establishes improved electrocatalytic ORR performances than the individual parent counterparts (i.e., CuO/C and CeO_2/C). It also exhibited high limiting current density and mass activity toward ORR. Furthermore, electrochemically this catalyst is capable of reducing O_2 to OH^- by a 4 e^- reduction mechanism in an alkaline solution. More importantly, $CuO/CeO_2/C$ shows a stable ORR performance which is comparable to the benchmark Pt/C. These excellences mainly originate from the boosted electrical conductivity, the adequate O_2 incorporation and transport abilities, high specific surface area and high ECSA and the synergistic effect between CuO, CeO_2 and carbon in the $CuO/CeO_2/C$ nanostructure. The fabrication strategy in this study introduces an insightful scope for designing low-cost, stable materials capable of driving high-performance ORR electrocatalysis for electrochemical devices.

References

[1] Yuan, C., Wu, H. B., Xie, Y., and Lou, X. W. Mixed transition-metal oxides: Design, synthesis, and energy-related applications. *Angewandte Chemie International Edition*, 53(6):1488-1504, 2014.

[2] Zhang, Z., Liu, J., Gu, J., Su, L., and Cheng, L. An overview of metal oxide materials as electrocatalysts and supports for polymer electrolyte fuel cells. *Energy & Environmental Science*, 7(8):2535-2558, 2014.

[3] Dresp, S., and Strasser, P. Non-Noble Metal oxides and their application as bifunctional catalyst in reversible fuel cells and rechargeable air batteries. *ChemCatChem*, 10(18):4162-4171, 2018.

[4] Xiao, H., Li, B., Zhao, M., Li, Y., Hu, T., Jia, J., and Wu, H. Electrosynthesized CuO_x/graphene by a four-electrode electrolysis system for the oxygen reduction reaction to hydrogen peroxide. *Chemical Communications*, 57:4118–4121, 2021.

[5] Yang, L. P., Mi, J. L., Liang, J. H., Zu, Z. Y., and Zhang, P. Copper–carbon: An efficient catalyst for oxygen reduction. *ACS Applied Energy Materials*, 2(9):6295-6301, 2019.

[6] Chen, J., Zhou, N., Wang, H., Peng, Z., Li, H., Tang, Y., and Liu, K. Synergistically enhanced oxygen reduction activity of MnO_x–CeO_2/Ketjenblack composites. *Chemical Communications*, 51(50):10123-10126, 2015.

[7] Yousaf, A. B., Imran, M., Uwitonze, N., Zeb, A., Zaidi, S. J., Ansari, T. M., Yasmeen, G. and Manzoor, S. Enhanced electrocatalytic performance of Pt_3Pd_1 alloys supported on CeO_2/C for methanol oxidation and oxygen reduction reactions. *The Journal of Physical Chemistry C*, 121(4):2069-2079, 2017.

[8] Masuda, T., Fukumitsu, H., Fugane, K., Togasaki, H., Matsumura, D., Tamura, K., Nishihata, Y., Yoshikawa, H., Kobayashi, K., Mori, T. and Uosaki, K. Role of cerium oxide in the enhancement of activity for the oxygen reduction reaction at Pt–CeO_x nanocomposite electrocatalyst-an in situ electrochemical X-ray absorption fine structure study. *The Journal of Physical Chemistry C*, 116(18): 10098-10102, 2012.

[9] Liu, K., Huang, X., Wang, H., Li, F., Tang, Y., Li, J., and Shao, M. Co_3O_4–CeO_2/C as a highly active electrocatalyst for oxygen reduction reaction in Al–air batteries. *ACS Applied Materials & Interfaces*, 8(50):34422-34430, 2016.

[10] Paulus, U. A., Schmidt, T. J., Gasteiger, H. A., and Behm, R. J. Oxygen reduction on a high-surface-area Pt/Vulcan carbon catalyst: A thin-film rotating ring-disk electrode study. *Journal of Electroanalytical Chemistry*, 495(2):134-145, 2001.

[11] Kuroda, S., Tobori, N., Sakuraba, M., and Sato, Y. Charge–discharge properties of a cathode prepared with ketjen black as the electro-conductive additive in lithium-ion batteries. *Journal of Power Sources*, 119:924-928, 2003.

[12] Li, W., Wang, X., Chen, Z., Waje, M., and Yan, Y. Carbon nanotube film by filtration as cathode catalyst support for proton-exchange membrane fuel cell. *Langmuir*, 21(21):9386-9389, 2005.

[13] Chen, L., Xu, X., Yang, W., and Jia, J. Recent advances in carbon-based electrocatalysts for oxygen reduction reaction. *Chinese Chemical Letters*, 31(3):626-634, 2020.

[14] Lee, J. S., Park, G. S., Lee, H. I., Kim, S. T., Cao, R., Liu, M., and Cho, J. Ketjenblack carbon supported amorphous manganese oxides nanowires as highly efficient electrocatalyst for oxygen reduction reaction in alkaline solutions. *Nano Letters*, 11(12):5362-5366, 2011.

[15] Jampaiah, D., Venkataswamy, P., Tur, K.M., Ippolito, S.J., Bhargava, S.K., and Reddy, B.M. Effect of MnO_x loading on structural, surface, and catalytic properties of CeO_2-MnO_x mixed oxides prepared by sol-gel method. *Zeitschrift für Anorganische und Allgemeine Chemie*, 641:1141–1149, 2015.

[16] McBride, J. R., Hass, K. C., Poindexter, B. D., and Weber, W. H. Raman and X-ray studies of $Ce_{1-x}RE_xO_{2-y}$, where RE= La, Pr, Nd, Eu, Gd, and Tb. *Journal of Applied Physics*, 76(4):2435-2441, 1994.

[17] Xu, J. F., Ji, W., Shen, Z. X., Li, W. S., Tang, S. H., Ye, X. R., Jia, D.Z. and Xin, X.Q. Raman spectra of CuO nanocrystals. *Journal of Raman Spectroscopy*, 30(5):413-415,(1999).

[18] Zhang, X., Wei, J., Yang, H., Liu, X., Liu, W., Zhang, C., and Yang, Y. One-pot synthesis of Mn-doped CeO_2 nanospheres for CO oxidation. *European Journal of Inorganic Chemistry*, 2013(25):4443-4449, 2013.

[19] Xu, C., Li, S., Zhang, Y., Li, Y., Zhou, J., and Qin, G. Synthesis of CuO_x–CeO_2 catalyst with high-density interfaces for selective oxidation of CO in H_2-rich stream. *International Journal of Hydrogen Energy*, 44(8):4156-4166, 2019.

[20] Qin, Y., Che, R., Liang, C., Zhang, J., & Wen, Z. Synthesis of Au and Au–CuO cubic microcages via an in situ sacrificial template approach. *Journal of Materials Chemistry*, 21(11):3960-3965, 2011.

[21] Wang, Z., Wang, W., Zhang, L., and Jiang, D. Surface oxygen vacancies on Co_3O_4 mediated catalytic formaldehyde oxidation at room temperature. *Catalysis Science & Technology*, 6(11):3845-3853, 2016.

[22] Nguyen, T. D., Dinh, C. T., and Do, T. O. Monodisperse samarium and cerium orthovanadate nanocrystals and metal oxidation states on the nanocrystal surface. *Langmuir*, 25(18):11142-11148, 2009.

[23] Zhang, L., and Shen, Y. One-pot synthesis of platinum–ceria/graphene nanosheet as advanced electrocatalysts for alcohol oxidation. *ChemElectroChem*, 2(6):887-895, 2015.

[24] Liang, R. N., Song, D. A., Zhang, R. M., & Qin, W. Potentiometric sensing of neutral species based on a uniform-sized molecularly imprinted polymer as a receptor. *Angewandte Chemie International Edition*, 49(14): 2556-2559, 2010.

[25] Xia, W., Mahmood, A., Liang, Z., Zou, R., and Guo, S. Earth-abundant nanomaterials for oxygen reduction. *Angewandte Chemie International Edition*, 55(8):2650-2676, 2016.

[26] Wang, M., Huang, J., Wang, M., Zhang, D., Zhang, W., Li, W., and Chen, J. Co_3O_4 nanorods decorated reduced graphene oxide composite for oxygen reduction reaction in alkaline electrolyte. *Electrochemistry Communications*, 34:299-303, 2013.